Acta Cryst. (1998). D**54**, 487–493

Miscellaneous Algorithms for Density Modification

Kevin Cowtan* and Peter Main

University of York, Heslington, York YO1 5DD, England. E-mail: cowtan@yorvic.york.ac.uk

(*Received 21 May 1997; accepted 9 September 1997*)

Abstract

Various algorithms are described, developed for the *dm* density modification package, which have not been described elsewhere. Methods are described for the following problems: determination of the absolute scale and overall temperature factor of a data set, by a method which is less dependent on data resolution than Wilson statistics; an efficient interpolation algorithm for averaging and its application to refinement of averaging operators; a method for the automatic determination of averaging masks.

1. Introduction

Since the paper of Wang (1985) phase improvement by density modification has become a routine part of the structure solution process. This success has been influenced by the automation of the calculations in a robust manner, and the use of fast and efficient algorithms. Density-modification methods by a number of authors have been implemented in the *dm* program (Cowtan, 1994), but the development required some additional algorithms for scaling, averaging and mask determination which are described here.

2. Scaling

Many density-modification and direct-methods techniques require the reduction of observed reflection data to an absolute scale (*i.e.* in electrons). In some cases (for example if *E*'s/*U*'s are required) it is necessary to calculate an overall temperature factor.

This has traditionally been accomplished through the use of Wilson statistics (Wilson, 1949), which provide an estimate of the expected mean scattered intensity at any scattering angle, based on the assumption of atoms placed randomly in a unit cell.

For small molecules this assumption works well, however for proteins it breaks down for two reasons.

(i) Minimum atomic separations mean that the atoms are not randomly distributed, at large scales they appear to be very uniformly distributed. The result of this is that low-resolution scattering (around 6 Å) is much weaker than predicted by Wilson statistics. The distribution of interatomic distances also lead to other features in the scattering curve (Blessing *et al.*, 1996).

(ii). Solvent voids within the protein cause long-range variations in the local mean density, leading to large features at very low resolutions (below 8 Å). These features are dependent on the shape of the solvent boundary, and vary in size in proportion to the contrast between the protein and solvent regions.

As a result, the Wilson curve may typically only be used to model the scattering from a protein at better than 5 Å resolution. Since the diffraction data may only extend to 3 Å or less and contain large errors at the resolution limit, any scale and/or temperature factor derived from it may contain large errors.

A better model can be constructed which represents at least the first class of features in the scattering curve. Instead of using a theoretically generated scattering curve, the scattering curves from a number of different structures, with atomic motion removed, are combined to form an empirical curve to which the observed data may be fitted. The curves must be normalized to account for the number of ordered scatterers in the unit cell, for almost all proteins this may be effectively estimated from the unit-cell volume and the solvent content.

The solvent is considered to contribute only to the origin reflection. In this way the method accounts for the uniformity of the atomic distribution (1) but neglects the shape of the solvent boundary (2). As a result, the scaling may typically be based on all the data higher than 8 Å, rather than the more typical 4–5 Å. Murshudov (1997) has suggested that when the solvent envelope is known this information may be used to further improve the empirical scaling curve.

By Parseval's theorem (see for example Bricogne, 1993*b*), the expected intensity in reciprocal space is linked directly to the variance of the scattering density in real space,

$$\sigma_\rho^2 = \frac{1}{V^2} \sum_{h \neq 000} |F(\mathbf{h})|^2. \qquad (1)$$

The protein scattering curve may then be calculated from the variance of the density within the protein region of a map, over a range of structures, at a range of resolutions. The expected scattered intensity within a particular resolution range is then given by the differ-

ISSN 0907-4449

Table 1. *Estimates for B and s using Wilson statistics and empirical curve at different resolutions*

Values from refined structure $\langle B \rangle = 50.2$, $s = 0.77$ using the *CCP*4 (Collaborative Computational Project, Number 4, 1994) *sfall* program.

Resolution limit (Å)	Wilson curve		Empirical curve	
	B	*s*	*B*	*s*
2.5	54.1	0.85	47.0	0.81
3.0	53.0	0.88	45.2	0.78
3.5	46.1	1.07	46.3	0.79
4.0	27.1	1.73	45.9	0.78
4.5	−19.6	4.68	48.4	0.80
5.0	—	—	58.9	0.87

ence in the variances of maps bounding that resolution range, with a correction for the shift in mean density due to solvent.

The averaged intensity scattering curve for protein density only, obtained over a range of protein structures, is shown in Fig. 1. Since the density of reflections in reciprocal space is proportional to the cell volume, this quantity is independent of the cell volume. Below 8 Å the curve begins to show envelope-specific features.

Possible improvements to the method include incorporation of information about the shape of the solvent boundary, and the inclusion of a typical range of thermal parameters over the atoms in the structure. The effect of the range of thermal parameters has been treated in some detail by Blessing *et al.* (1996), however it is not immediately useful for density modification because the thermal-parameter range is not modelled in current histogram-matching techniques, and often the data resolution is insufficient to determine the extra parameter.

In order to calculate the scale factor required to bring the data onto an absolute scale, the parameters *B* and *s* must be determined. The values are calculated which give the best fit between a theoretical scattering curve (either from Wilson statistics or the empirical method described above) and the experimental data.

$$|F_{\text{absolute}}|^2 = s|F_{\text{obs}}|^2 \exp[2B \sin^2(\theta)/\lambda^2]. \qquad (2)$$

A test data set, O^6-methylguanine-DNA-methyltransferase (Moore *et al.*, 1994), was used to compare the methods. Experimental data was available to 2.4 Å resolution, but the data was truncated at various resolutions, and the parameters *B* and *s* estimated by both methods. The Wilson plot for this data is roughly linear in the resolution range 5.0–2.4 Å, therefore, only data at higher than 5 Å were used for scaling against the Wilson curve. All the data was used for scaling against the empirical curve. The results are shown in Table 1.

Note that the estimates of *B* and *s* using the empirical curve are insensitive to the data resolution when it is better than 4.5 Å. In contrast, the Wilson curve cannot be calculated at 5 Å or less and gives misleading results at less than 4.0 Å and the scale factor *s* only approaches the empirical curve estimate at high resolution.

The scaling parameters determined by this method have proven effective both for histogram matching and Sayre's equation as employed by Zhang & Main (1990). Once the data has been put on an absolute scale, the origin $F(000)$ term can be calculated from the number of electrons in the unit cell. This estimate has proven sufficiently accurate in our tests for the calculation of maximum-entropy centroid maps (Bricogne, 1993*a*).

3. Interpolation

The efficiency of the *FFT* algorithm means that it is normal to calculate electron-density maps on uniformly sampled grids. However, some calculations, including the averaging of regions of the density map related by non-crystallographic symmetry (NCS), require the value of the density at points away from the grid sites. Rather than calculating density values by direct Fourier summation, it is efficient to perform a grid-based *FFT* and then interpolate for the density at the required position.

The choice of an effective interpolant presents problems. The simplest function, tri-linear interpolation, involves a linear combination of the densities at the eight grid points at the corners of a box enclosing the required coordinate. The interpolated density, however, fails to represent peaks between grid points and is not continuously differentiable. Another common interpolant is 64-point tri-cubic interpolation, or a faster 32-point approximation. This function is much slower to compute.

A better solution to the interpolation problem can be found in the family of *b*-splines, which are the self-convolutions of the top-hat function, defined as follows,

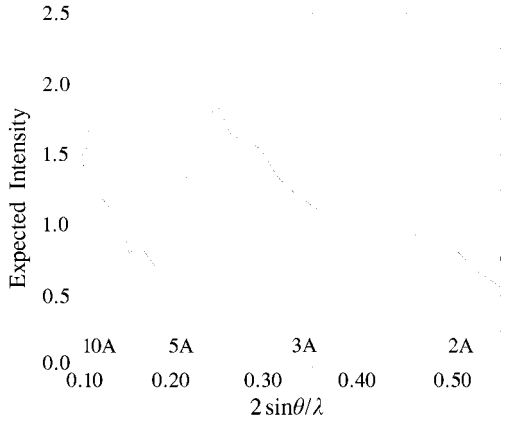

Fig. 1. Expected intensity over volume as a function of resolution for a protein only structure in $(e^-)^2$ Å^{-3}.

Table 2. *Comparison of interpolation methods*

Interpolation method	Number of points
Linear	8
Cubic (approx.)	32
Linear *b*-spline (b_1)	8
Quadratic *b*-spline (b_2)	27

$$b_0(x) = 1 \quad (-1/2 < 1/2)$$
$$0 \quad \text{(otherwise)}, \tag{3}$$

$$b_m(x) = \int_{-\infty}^{\infty} b_0(y) b_{m-1}(x-y)\mathrm{d}y. \tag{4}$$

The first three *b*-splines are shown in Fig. 2. Note that the linear *b*-spline b_1 is composed of two linear segments, the quadratic *b*-spline b_2 is composed of three quadratic segments.

Since the *b*-splines are constructed by self-convolution, their Fourier transforms take on particularly simple forms. The Fourier transform of b_0 is the sync-function, $\sin(\pi s)/\pi s$ where s is the coordinate in Fourier space. Since convolution of the *b*-splines corresponds to the multiplication of their Fourier coefficients, the Fourier transform of b_m is $[\sin(\pi s)/\pi s]^{m+1}$.

The application of these functions to interpolation is hinted at by Bricogne (1974) and has been developed by Grosse & Hobby (1994). Interpolation can be treated as a weighted summation of the density at grid points around the target coordinate.

It is possible to use the *b*-splines as weighting functions for interpolation. For example, convolution of the grid density with b_0 is equivalent to taking the density from the nearest grid point to the target point. Convolution with b_1 corresponds to linear interpolation. Since this is equivalent to multiplying the map coefficients by sync-functions in reciprocal space, it can be seen that using the *b*-splines as interpolants will produce a smoothed density map.

To obtain a better interpolated density, the map should be sharpened by the same amount that it is smoothed by interpolation. Thus, instead of interpolating from the density map itself, the Fourier coefficients of the map (structure factors) are first divided by the Fourier coefficients of the *b*-spline $[\sin(\pi s)/\pi s]^{m+1}$, to produce a sharpened map.

In three dimensions, interpolation can be performed by interpolating along each of the three grid directions in turn, or equivalently by convolution with a three-dimensional function constructed from the product of the three one-dimensional *b*-splines. The sharpening function in reciprocal space correction is the product of the three sync-functions. Non-orthogonal grids present no problem, since the distortion of the convolution function is compensated for by the distortion of the sharpening function in reciprocal space. However, care is required in hexagonal space groups, since in this case (only) structure factors which are symmetry equivalent can require different sharpening coefficients. If the sharpening is performed in $P1$, then this problem never arises.

In three dimensions, the full calculation is described as follows,

$$F_b(h,k,l) = F(h,k,l) \times \left[\frac{\sin(\pi h/n_u)}{\pi h/n_u}\frac{\sin(\pi k/n_v)}{\pi k/n_v}\frac{\sin(\pi l/n_w)}{\pi l/n_w}\right]^{m+1}, \tag{5}$$

$$\rho_b(u_1, v_1, w_1) = \mathrm{FFT}[F_b(h,k,l)], \tag{6}$$

$$\rho_{\mathrm{int}}(u,v,w) = \sum_{u_1}\sum_{v_1}\sum_{w_1} b_m[n_u(u_1-u)]b_m[n_v(v_1-v)] \times b_m[n_w(w_1-w)]\rho_b(u_1,v_1,w_1), \tag{7}$$

where u_1, v_1, w_1 take values in the range 0–1 on a grid of sampling n_u, n_v, n_w. (7) may be factorized for efficient computation.

A detailed comparison has been made between linear and quadratic *b*-splines (b_1 and b_2) and two other interpolation methods: conventional linear interpolation and 32-point cubic interpolation. Density values are calculated for points chosen at random in the unit cell, first by direct Fourier summation, then by each of the interpolation methods. The correlation between the exact Fourier values and the interpolated values gives a measure of the quality of the interpolating function. The relationship of the standard deviations of the two samples gives some idea of the degree of smoothing caused by interpolating. The time taken by each method varies roughly as the number of density values included as shown in Table 2.

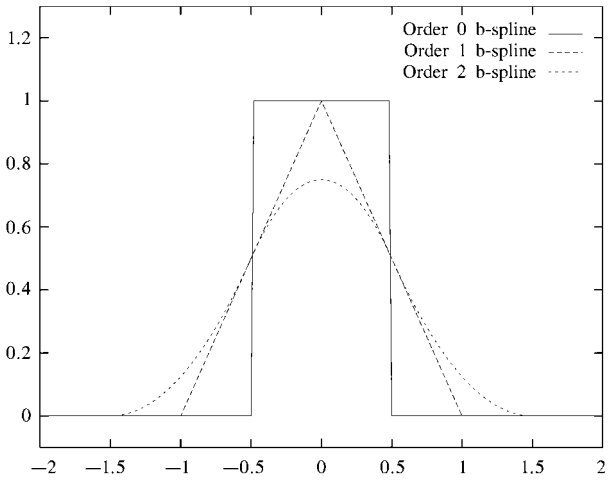

Fig. 2. *b*-Splines order 0, 1 and 2.

Tests were conducted using O^6-methylguanine-DNA-methyltransferase (Moore *et al.*, 1994) which has an orthorhombic unit cell, although tests in monoclinic and hexagonal space groups yield very similar results. As a stringent test, maps were calculated from the refined structures, and the corresponding structure factors sharpened to give $B_{\text{overall}} = 0$.

In Fig. 3(*a*), the correlation coefficient between the Fourier density and the interpolated density is shown for different samplings of the source grid, expressed in terms of Shannon rate (the ratio of the Nyquist spacing for the data to the grid spacing, see for example Beauchamp & Yuen, 1979). Thus, a Shannon rate of 1 is the coarsest grid on which a map may be calculated at a particular resolution, and Shannon rate of 2 is a grid twice as fine in each direction.

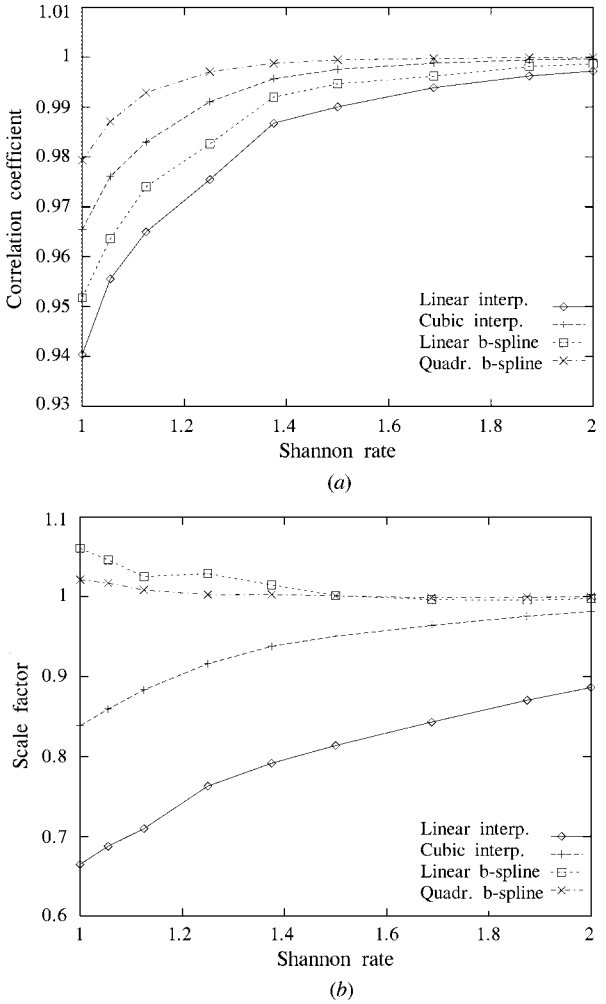

Fig. 3. Comparison between interpolated and direct-Fourier density with Shannon rate. (*a*) Correlation between interpolated and Fourier density. (*b*) Scale factor between interpolated and Fourier density.

On a fine grid, the functions all perform well, however when the initial grid is coarse, the sharpening of the data in reciprocal space leads to significantly better results. The quadratic *b*-spline gives significantly better interpolation than the cubic interpolant, and the linear *b*-spline gives better interpolation than simple linear interpolation.

To estimate how much smoothing of the map takes place during the interpolation calculation, the standard deviations of interpolated values (formed as part of the correlation coefficient) were compared with the Fourier values. The results are shown in Fig. 3(*b*). Note that the linear and cubic interpolation schemes both smooth the map badly at low Shannon rates. The reciprocal space sharpening in the *b*-spline case successfully corrects for this smoothing. At low Shannon rates the maps are very slightly over sharpened.

b-Splines have also been applied to the contouring of maps on fine grids by Ten Eyck *et al.* (1997).

3.1. *Refinement of averaging operators*

The *b*-spline interpolation method can also be applied in the refinement of the transformation matrices representing the NCS operations. This is normally performed by adjusting the averaging operator (expressed in Euler angles, for example) to maximize the correlation between related areas of density.

This can be efficiently achieved using a minimization technique, with steps taken in the direction of the gradient of the correlation function with respect to the six parameters describing the symmetry operation; *i.e.* three rotational and three translational parameters.

Using the quadratic *b*-spline, the derivatives of the density at a point can be simply calculated with respect to the grid axes by replacing the *b*-spline b_2 along that axis with its derivative b_2' (consisting of three linear segments). Thus, the gradient along the u direction can be calculated as,

$$\frac{\partial \rho}{\partial u}(u, v, w) = \sum_{u_1}\sum_{v_1}\sum_{w_1} b_2'[n_u(u_1 - u)]b_2[n_v(v_1 - v)] \times b_2[n_w(w_1 - w)]\rho_b(u_1, v_1, w_1), \tag{8}$$

(and similarly for v and w). It is computationally efficient to calculate the interpolated density value and the gradients simultaneously.

The gradient along an arbitrary coordinate direction may be obtained from a set of orthogonal gradients by application of the chain rule, however in the case of a non-orthogonal grid the gradients along grid directions are not independent. An intermediate set of orthogonal gradients must therefore be constructed.

Let the orthogonal angstrom vector $\mathbf{x}_i$ be related to the fractional vector $\mathbf{u}_j$ by the orthogonalization matrix q_{ij}, whose inverse matrix is the fractionalization matrix

Q_{ij}. Therefore,

$$\mathbf{x}_i = \sum_{j=1,3} q_{ij} u_j \quad i = 1, 3, \tag{9}$$

$$\mathbf{u}_i = \sum_{j=1,3} Q_{ij} x_j. \tag{10}$$

Then, by the chain rule,

$$\frac{\partial \rho}{\partial u_i} = \sum_{j=1,3} \frac{\partial x_j}{\partial u_i} \frac{\partial \rho}{\partial x_j} = \sum_{j=1,3} q_{ji} \frac{\partial \rho}{\partial x_j}, \tag{11}$$

and by inversion,

$$\frac{\partial \rho}{\partial x_i} = \sum_{j=1,3} Q_{ji} \frac{\partial \rho}{\partial u_j}. \tag{12}$$

Thus, the orthogonal gradients can be obtained from the fractional gradients by application of the transpose of the fractionalization matrix.

Once the gradients of the density with respect to the orthogonal axes are known, the derivatives with respect to the six parameters of the averaging operator r_i (three rotation and three translation) describing the symmetry operator can be derived by application of the chain rule,

$$\frac{\partial \rho}{\partial r_i} = \sum_{j=1,3} \frac{\partial x_j}{\partial r_i} \frac{\partial \rho}{\partial x_j} \quad i = 1, 6 \tag{13}$$

where the derivatives $\partial x_j / \partial r_i$ will depend on the choice of parameters r_i for the averaging operator. The derivative of the correlation $\mathcal{C}$ of the electron densities follows directly,

$$\mathcal{C} = \frac{\overline{\rho \rho_{\text{rot}}} - \overline{\rho}\ \overline{\rho_{\text{rot}}}}{[(\overline{\rho^2} - \overline{\rho}^2)(\overline{\rho_{\text{rot}}^2} - \overline{\rho_{\text{rot}}}^2)]^{1/2}} \tag{14}$$

$$\frac{\partial \mathcal{C}}{\partial r_i} = \frac{\overline{\rho \frac{\partial \rho_{\text{rot}}}{\partial r_i}} - \overline{\rho}\ \overline{\frac{\partial \rho_{\text{rot}}}{\partial r_i}}}{[(\overline{\rho^2} - \overline{\rho}^2)(\overline{\rho_{\text{rot}}^2} - \overline{\rho_{\text{rot}}}^2)]^{1/2}}, \tag{15}$$

where ρ is the untransformed density, ρ_{rot} is the transformed density, and the averages are calculated over the volume of the averaging mask. (The standard deviation of the rotated density in the denominator is assumed to be constant.) The actual refinement procedure is performed by calculating the gradient of the correlation with respect to the six parameters. The components of this gradient give the direction for adjusting the parameters. A three-point line search is then performed along this direction to determine the actual shifts to apply to each of the parameters.

4. Automatic NCS mask determination

Averaging is one of the most powerful constraints available for phase improvement, however it is also the least automatic. While the determination of a solvent mask is routinely automated (Wang, 1985), the process of generating an averaging mask delimiting that volume of crystal space which obeys the NCS operators is still often achieved by laborious use of a graphics package.

Some progress has been made towards automation using the local density correlation function between regions of density related by the averaging operator to distinguish the volume over which that operator applies (Vellieux *et al.*, 1995). The full automation of this method for simple cases is described here (a similar method, unpublished, has been developed by Volbeda, 1997).

The local correlation function gives the agreement between the unrotated and rotated maps as a function of position,

$$\mathcal{C}(x) = \frac{\langle \rho \rho_{\text{rot}} \rangle_x - \langle \rho \rangle_x \langle \rho_{\text{rot}} \rangle_x}{(\langle \rho^2 \rangle_x - \langle \rho \rangle_x^2)(\langle \rho_{\text{rot}}^2 \rangle_x - \langle \rho_{\text{rot}} \rangle_x^2)]^{1/2}} \tag{16}$$

where $\langle\ \rangle_x$ represents an average calculated over a sphere around the point x. A number of difficulties exist in the generation of an averaging mask from a local correlation map.

(i) Proper/improper symmetry. If the NCS forms a closed group (a proper symmetry), then the NCS operators will map the whole of the multimer onto itself, thus the local correlation will be high over the whole of the multimer. If the NCS forms an open group (improper symmetry), then each operator will only map a monomer onto one other, therefore the local correlation will only be high over a monomer. Mixed symmetries are also possible.

(ii) The averaging mask does not obey crystallographic symmetry or cell repeat, rather it is defined precisely once in crystal space. It must, therefore, be represented over that volume in real space; it may be larger than the cell in some direction, and will not normally fall within the volume (u,v,w) = (0...1,0...1,0...1).

(iii) If an NCS operator lies perpendicular to a special direction, then the mask may repeat along that special direction. Thus, for example, a twofold NCS axis perpendicular to a twofold crystallographic axis leads to a mask which repeats along the crystallographic axis. In this case arbitrary limits must be placed on the mask extent along this axis.

4.1. *Method*

The method is divided into three steps.

4.1.1. *Calculation of local correlations*. For speed, correlations are calculated on a coarse search grid. A sphere is constructed about each search grid point, and density values calculated for unrotated and rotated maps on a fine grid within that sphere. The fine grid is at twice the Nyquist spacing (*i.e.* at 2.0 Å resolution the

fine grid has 2.0 Å spacing). The radius of the sphere is then chosen to cover about 400 points, and the local correlation is calculated over these points. Initially the grid is much larger than a unit cell, typically (−1...2,−1...2,−1...2) in fractional coordinates.

4.1.2. *Masking*. A cutoff level is chosen so that if all points above the cutoff level are within the mask, the expected volume of the monomer of multimer will be enclosed. The correlation map is then converted into a mask with this cutoff.

4.1.3. *Mask continuity testing*. All the separate contiguous volumes within the mask are identified. The largest single connected volume is isolated. The bounds of the correlation grid are then reset to enclose this volume, with a generous border (Fig. 4).

This process is repeated over four cycles, after which the correlation grid bounds have been reduced sufficiently to give a detailed mask outline. Some indication of a successful mask determination is obtained from the number and size of the separate masked features at each stage, if the mask consistently features one volume much larger than any others, then it is probably correct.

The calculation of correlations around every grid point on the search grid can be very time consuming. In practice it has been found to be sufficient to calculate correlations only at every second or third grid point along each axis, and then generate the rest by linear interpolation. This reduces the computational requirement by 1/8 or 1/27.

In the case of NCS axes along special directions, the user must specify limits to the search box along a particular cell axis. These limits are then fixed for the whole calculation. This is not a complete solution, but does account for the most common cases.

An example auto-mask, calculated using RNAse (Ševčík *et al.*, 1991) MIR data, is shown here. The structure has twofold improper NCS, thus the local-correlation mask covers only one monomer. The molecule and the mask are shown in Fig. 5. In this case the mask closely follows the boundaries of the protein, with only one loop and a few side chains outside the mask. The technique appears to be insensitive to the quality of the map, however, for very poor starting maps (*e.g.* SIR or OAS) it is sometimes necessary to increase the number of points included in the local correlation sphere.

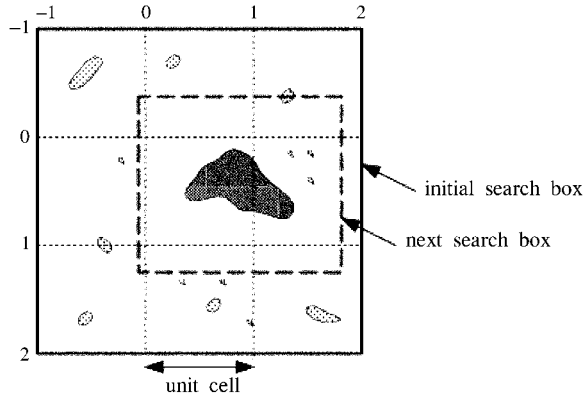

Fig. 4. Largest connected volume identification and grid rescaling in the automatic NCS-masking calculation.

5. Conclusions

Density modification is now a routine part of structure solution, often using the algorithms described here. A scaling algorithm using all the data, which is robust against limited data resolution and detailed features of the scattering curve, allows the reliable application of histogram matching without human intervention. High-speed interpolation from coarse map grids also means that averaging operator refinement may be applied automatically at every stage of the phase-improvement calculation, and also allows the use of exhaustive search methods for averaging mask determination rather than the painstaking analysis of operators and density using computer graphics.

Examples of structure solutions using the *dm* program and a multi-crystal version include the GTPase-activating domain from p50rhoGAP (Barrett *et al.*, 1997), and the cofactor-binding fragment of the LysR family member CysB (Tyrrell *et al.*, 1998).

The authors would like to thank Eric Grosse for advice on *b*-splines and Dave Schuller and Fred Vellieux for helpful discussions on averaging

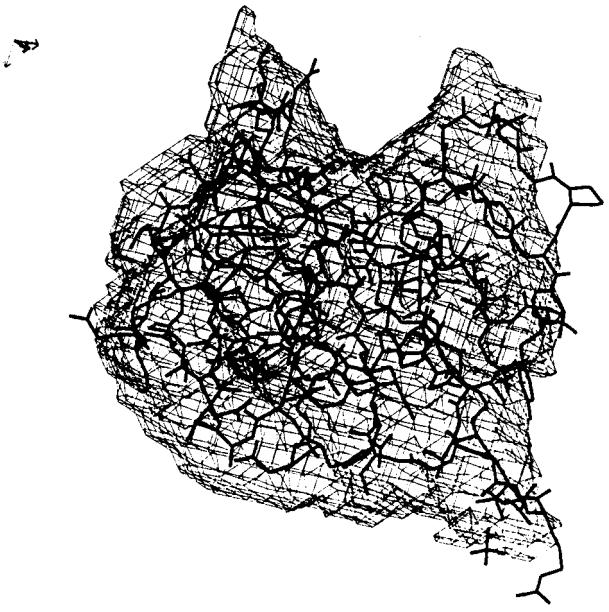

Fig. 5. Auto-NCS mask calculated for RNAse using MIR data.

calculations and masks. Dr Cowtan is grateful to the United Kingdom BBSRC (grant number 87/B03785) and the *CCP*4 project for supporting this work.

References

Barrett, T., Xiao, B., Dodson, E. J., Dodson, G. G., Ludbrook, S. B., Nurmahomed, K., Gamblin, S. J., Musacchio, A., Smerdon, S. J. & Eccleston, J. F. (1997). *Nature (London)*, **385**, 458–461.

Beauchamp, K. G. & Yuen, C. K. (1979). *Digital Methods for Signal Analysis*. London: George, Allen & Unwin Ltd.

Blessing, R. H., Guo, D. Y. & Langs, D. A. (1996). *Acta Cryst.* D**52**, 257–266.

Bricogne, G. (1974). *Acta Cryst.* A**30**, 395–405.

Bricogne, G. (1993*a*). *Acta Cryst.* D**49**, 37–60.

Bricogne, G. (1993*b*). *International Tables for Crystallography* Vol. *B*, edited by U. Shmueli, pp. 23-106. Dordrecht: Kluwer Academic Publishers.

Collaborative Computational Project, Number 4 (1994). *Acta Cryst.* D**50**, 760–763.

Cowtan, K. (1994). *Jnt CCP4 ESF-EACBM Newslett. Protein Crystallogr.* **31**, 34–38.

Grosse, E. & Hobby, J. D. (1994). *Math. Comput.* **63**, 175–194.

Moore, M. H., Gulbis, J. M., Dodson, E. J., Demple, B. & Moody P. C. E. (1994). *EMBO J.* **13**, 1495–1501.

Murshudov, G. (1997). Personal communication.

Ševčík, J., Dodson, E. & Dodson, G. G. (1991). *Acta Cryst.* B**47**, 240–253.

Ten Eyck, L. F., Nelson, E. & McRee, D. E. (1997). Personal communication.

Tyrrell, R., Verschueren, K. H. G., Dodson, E. J., Murshudov, G. N., Addy, C. & Wilkinson, A. J. (1998). *Structure*. In the press.

Vellieux, F. M. D. A. P., Hunt, J. F., Roy, S. & Read, R. J. (1995). *J. Appl. Cryst.* **28**, 347–351.

Volbeda, A. (1997). Personal communication.

Wang, B.-C. (1985). *Methods Enzymol.* **115**, 90–112.

Wilson, A. J. C. (1949). *Acta Cryst.* **2**, 318–321.

Zhang, K. Y. J. & Main, P. (1990). *Acta Cryst.* A**46**, 377–381.